Published in partnership with FCT NOVA with the support of E-MRS



https://doi.org/10.1038/s41699-025-00565-1

Anisotropic screening of excitons in van der Waals materials



Ting-Hsuan Wu¹, Chih-En Hsu², Rajesh Kumar Ulaganathan⁴, Raman Sankar¹, Zhenglu Li³, Chi-Cheng Lee², Chia-Seng Chang¹ & Kung-Hsuan Lin¹,5,6 ⋈

Van der Waals (vdW) materials exhibit optical anisotropy due to the fundamental difference between in-plane (IP) covalent bonds and out-of-plane (OP) vdW bonds. In particular, InSe, a vdW material, provides an excellent platform for studying the optical properties of anisotropic excitons. We measure the energy difference between excitons with IP and OP dipole responses in InSe to be 0.4 meV. Under photoexcitation with femtosecond pulses, the photocarriers screen the excitons and can increase the energy difference between IP and OP optical responses to as much as 8 meV. This energy difference results from the varying screening lengths along the IP and OP directions. The change in energy difference persists for over 100 ps at 77 K, but recovers much faster, within 100 ps, at room temperature. The dependence of carrier density on the anisotropic screening of excitons has also been investigated.

Anisotropic excitons offer great potential for manipulating light-matter interactions in two-dimensional (2D) optoelectronic and photonic applications. Their formation is influenced by their optical transition dipole moments, which are governed by optical selection rules^{1,2} and electronic properties under various symmetry operations^{3,4}, leading to different exciton oscillator strengths. Hence, excitons can exhibit different optical responses depending on the in-plane (IP), out-of-plane (OP), and mixed orientations of optical polarizations^{2,5-8}. Most devices, based on 2D or van der Waals (vdW) materials such as transition metal dichalcogenides (TMDs)⁹⁻¹¹, rely on materials with IP dipole orientation, which can easily interact with light at normal incidence and promote directional outcoupling of radiation^{5,9,12}. However, in emerging applications such as optical communications^{13,14}, plasmonic nanocavities^{15,16}, and radially polarized sources¹⁷, the presence of OP dipole orientation, which requires the polarization of light in the IP direction, is crucial for efficient control of lightmatter interactions.

Recently, indium selenide (InSe), a type of vdW III–VI chalcogenide, has attracted increasing attention due to its strong luminescence from excitons with OP dipole orientation ^{8,16,18–21}. In addition, it demonstrates high carrier mobility of ~10³ cm²/V-s at room temperature (RT)²², showing promising potential for applications in electronic, nanophotonic and optoelectronic devices, such as field-effect transistors^{22–24}, photodetectors^{25,26}, nanocavity¹⁵, and mechanical and gas sensors^{24,27}. The OP dipole orientation in InSe arises from the transition between the lowest

conduction band (CB), primarily dominated by the s orbital of the In atom, and the highest valence (VB), mainly dominated by the p_z orbital of the Se atom^{19,20}. However, the IP dipole orientation also mixes with this transition near the band edge due to spin-orbit coupling (SOC)⁸. Experimentally, the bandgap luminescence dominated by OP dipole orientation has been confirmed by luminescence enhancement in the ridge and bent regions of InSe^{18-21,28}. Exciton emission of InSe in the plasmonic nanocavity can also be significantly enhanced through effective exciton-plasmon interaction in the z-direction¹⁶. The relative contributions of IP and OP dipole orientations to exciton luminescence have been quantitatively determined by analyzing the far-field intensity distribution of polarization-resolved photoluminescence (PL) using a high-NA objective lens⁸. Consequently, InSe provides an excellent platform for studying the optical properties of anisotropic excitons.

Previous work reported the anisotropic responses of exciton luminescence intensity in InSe; however, anisotropy in energy was not observed. In this study, we utilize obliquely incident and polarization-resolved light to investigate the IP and OP optical features of InSe. The energy difference between IP and OP optical responses from excitons in InSe was experimentally resolved to be ~0.4 meV. The theoretical results indicate that the contributions of excitons with IP and OP responses originate from different k-points and split states. Under photoexcitation by femtosecond pulses, the energy difference of IP and OP optical responses can increase to as much as 8 meV. The time-resolved energy difference could last over 100 ps at 77 K. A similar energy difference was also observed at RT, but became

¹Institute of Physics, Academia Sinica, Taipei, Taiwan. ²Department of Physics, Tamkang University, Tamsui, New Taipei, Taiwan. ³Mork Family Department of Chemical Engineering and Materials Science, University of Southern California, University of Southern California, Los Angeles, CA, USA. ⁴Centre for Nanotechnology, Indian Institute of Technology, Roorkee, India. ⁵Taiwan Consortium of Emergent Crystalline Materials, National Science and Technology Council, Taipei, Taiwan. ⁶Graduate Institute of Applied Physics, National Chengchi University, Taipei, Taiwan. ⊠e-mail: linkh@sinica.edu.tw

indistinguishable after 100 ps. The peaks of time-integrating exciton PL for IP and OP polarizations are not identical either. The difference in peak energy between IP and OP polarizations increases with increasing laser power (or carrier density). The anisotropic responses in energy result from differences in the screening effects of photocarriers on excitons along the IP and OP directions. Anisotropic screening of excitons in InSe was observed because the fundamental difference between IP covalent and OP vdW bonds in vdW materials leads to optical anisotropy in dielectric constants^{29,30}.

Results

Electronic and optical properties of y-InSe

The properties of y-InSe were theoretically investigated using firstprinciples methods, including many-body effects. Details of the calculation information are provided in the Methods section. γ-InSe consists of a stacking sequence of three layers along the OP (or z) direction, as shown in Fig. 1a. Figure 1b presents the theoretical absorption spectra calculated using the GW and GW plus Bethe-Salpeter-equation (GW-BSE) approaches, with the polar angle of polarization varying between 0° (IP, along the x axis) and 90° (OP, along the z-axis). The absorption with OP polarization is the strongest and decreases as the polar angle sweeps from 90° to 0° (the IP direction). The first absorption peak for 0° occurs at 1.2800 eV, representing the lowest energy of IP excitonic states, while the peak for 90° appears at 1.2796 eV, representing the lowest energy of OP excitonic states. The two responses for different polarizations (IP and OP) are nearly degenerate within the current theoretical framework. However, the absorption of light with OP polarization is significantly stronger than with IP polarization, meaning that the absorption features for angles between 90° to 0° are dominated by the characteristics of OP absorption.

Transmission measurements were performed at an obliquely incident angle of ~22° to obtain the absorption spectra of γ -InSe flakes. A polarizer was used for light source with either S- or P-polarization. The experimental configuration is detailed in the Methods section. In Fig. 1c, the absorption peaks for P-polarized and S-polarized light at 5 K are 1.3378 eV and 1.3374 eV, respectively. The P-polarized spectra are assumed to predominantly reflect OP exciton absorption features. Consequently, this indicates that the OP excitonic energy is 0.4 meV higher than the IP excitonic energy. The energy difference (ΔE) between the two excitonic peaks is independent of the temperature (Supplementary Fig. 1). The inset of Fig. 1c highlights the excited states (n=2) of the excitons. The binding energies of exciton for the IP response $R_{\rm ex,IP}$ and OP response $R_{\rm ex,OP}$ were experimentally determined to be 15.1 meV and 14.5 meV, respectively, based on the ground state (n=1) and excited state (n=2) of the direct exciton series 31,32 .

Figure 1d illustrates the dominant electron states contributing to absorption near the band edges around the high symmetry point T in the Brillouin zone (BZ). The band splitting due to SOC occurs only along the IP direction (T \rightarrow H2)³³. The lowest CB and the highest VB each split into two bands, namely, the lower c_1 and the higher c_2 for the CB, and the higher v_1 and the lower v_2 for the VB. The GW-calculated bandgap is 1.2910 eV. The calculated $R_{\rm ex,IP}$ and $R_{\rm ex,OP}$, derived from the difference between the bandgap and the lowest exciton energy, are 11.0 meV and 11.4 meV, respectively. These calculated results align well with the experimental data within the margin of uncertainty. Notably, the difference between the IP and OP excitonic states arises only when SOC is included in the calculations. To further explore the origin of the OP and IP excitonic states, the intensities of the exciton envelope functions $\left|A_{vc}^{\rm IP}\right|^2$ and $\left|A_{vc}^{\rm OP}\right|^2$ are plotted in Fig. 1e, f, respectively. Here, the subscripts v and c denote the valence and CBs. The exciton envelope function describes the eigenvector of the BSE Hamilton in

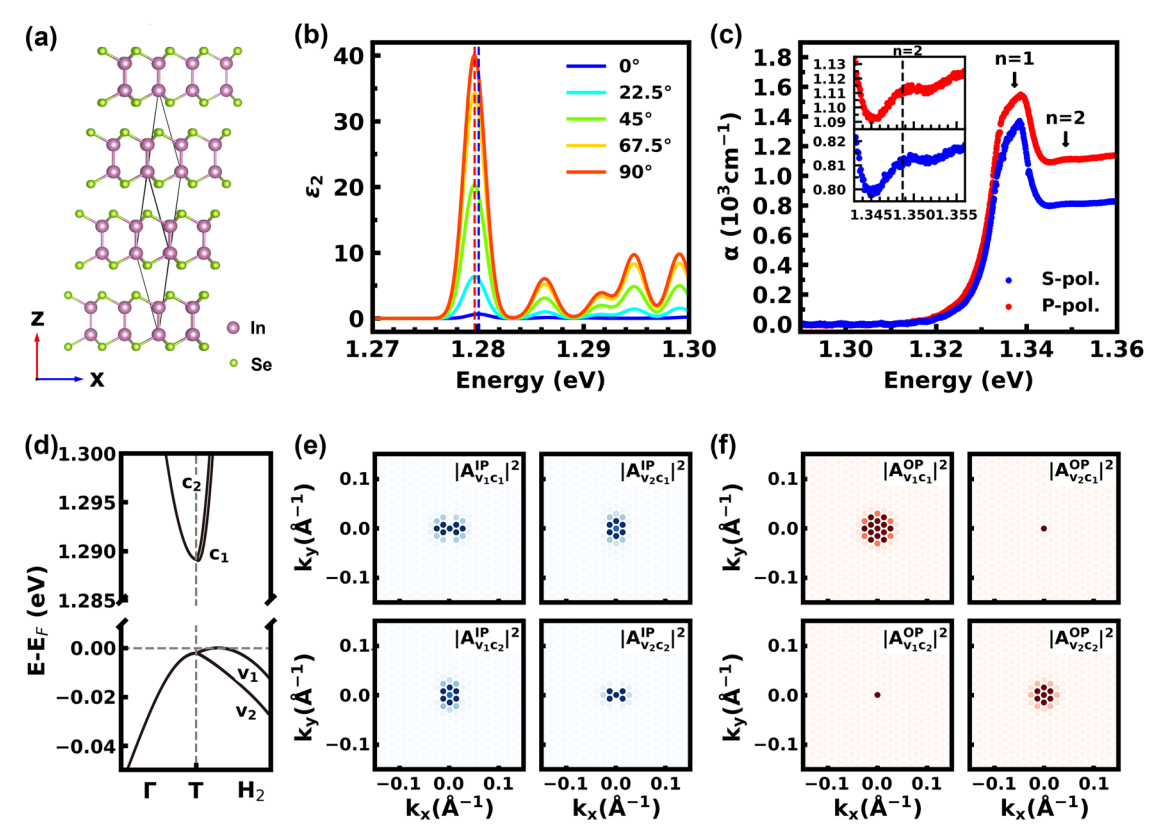
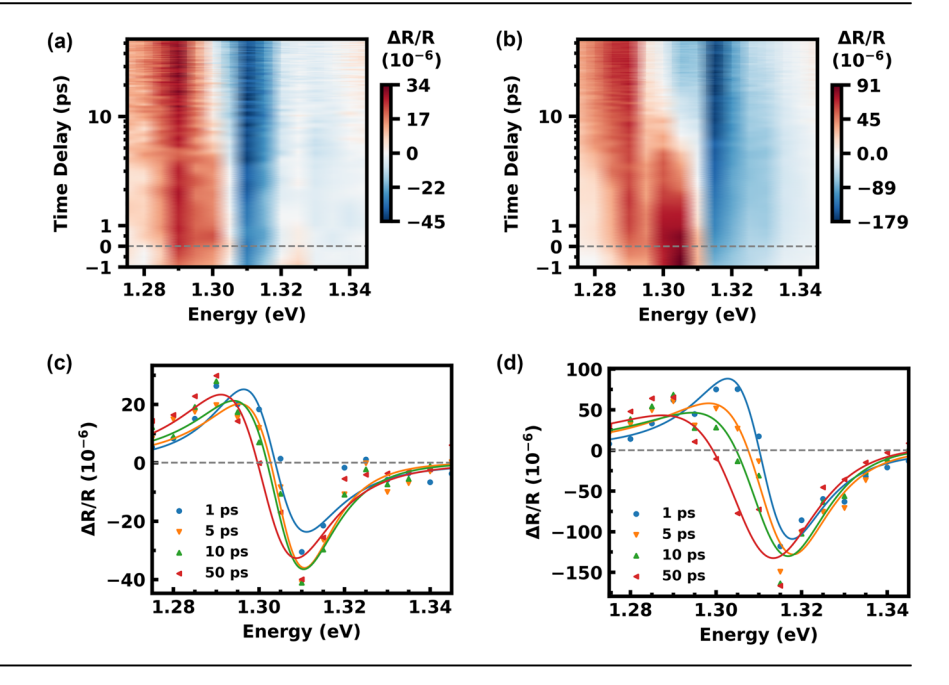


Fig. 1 | **Electronic and optical properties of γ-InSe. a** Crystal structure of γ -InSe. The solid line shows the primitive unit cell. **b** Polarization-dependent absorption spectra. The angle represents the polar angle of the polarization with respect to the atomic plane of the structure. **c** Experimental absorption spectra at ~5 K. The inset

highlights the excitonic peaks for n = 2. **d** Band structure near the band edges. **e** and $\mathbf{f} \left| A_{vc}^{\mathrm{IP}} \right|^2$ and $\left| A_{vc}^{\mathrm{OP}} \right|^2$ represent the distribution of envelope functions contributing to the lowest excitonic peaks for IP (0°) and OP (90°) polarization in (**b**), respectively. The center of 2D map is at (0, 0, 0.377 A⁻¹), the T point.

Fig. 2 | TR spectra of InSe at 77 K probed with different polarizations. The carrier density is 1.43×10^{17} cm⁻³. Pseudocolor 2D map of reflectivity changes as a function of energy and time with a S-and b P-polarized probe. The gray dashed lines indicate time zero. c S- and d P-polarized reflectivity change spectra at delay times of 1 ps, 5 ps, 10 ps, and 50 ps. The dots represent the experimental data, while the solid lines show the fitting results.



the basis of Bloch wavefunctions, specifically v_1 , v_2 , c_1 , c_2 as shown in Fig. 1d, in k-space. The four $\left|A_{vc}^{OP}\right|^2$ functions responsible for the OP excitonic peak at 1.2796 eV in Fig. 1b show isotropic distributions in BZ, whereas the four $\left|A_{vc}^{IP}\right|^2$ functions for the IP peak at 1.2800 eV are anisotropic around the T point. This indicates that the contributions of excitons with IP and OP responses originate from different k-points and split states.

Ultrafast dynamics of IP and OP optical transitions at low temperature

Oblique transient reflection (TR) spectroscopy was employed to investigate the ultrafast exciton dynamics in γ -InSe. The sample temperature was cooled to 77 K, corresponding to a thermal energy of 6.6 meV, which is lower than the exciton binding energy. The energy of P-polarized pump beam was fixed at 3.1 eV, while the broadband probe beam, either S- or Ppolarized, was used for the measurements. Details of the experimental setup are provided in the Methods section. Figure 2a, b present pseudocolor 2D maps showing the $\Delta R/R$ spectra at different time delays for S- and P-polarized probes, respectively. Notably, the $\Delta R/R$ signal for the P-polarized probe is ~3.5 times stronger than that of the S-polarized probe. It is important to note that all experimental conditions were identical for both measurements, except for the half-wave plate, which was rotated to adjust the probe polarization. The higher sensitivity observed for the P-polarized probe is attributed to the greater absorption in OP polarization. In both 2D maps, the $\Delta R/R$ signal exhibits a significant shift from positive values (red) to negative values (blue) around the resonant transition energy. The energy at which $\Delta R/R = 0$ (white) corresponds approximately to the resonant energy.

Figure 2c, d display the spectral responses for the different polarized probes at 1 ps, 5 ps, 10 ps, and 50 ps, extracted from Fig. 2a, b, respectively. To quantitatively analyze the time evolution of the resonant energy, these responses were fitted using a photoreflectance model³⁴. This model accounts for the real part of the dielectric function, which exhibits a first-derivative Lorentzian line shape,

$$\frac{\Delta R}{R} = Re \left[A e^{i\phi} \left(E - E_{Opt} + i\Gamma \right)^{-2} \right], \tag{1}$$

where A is the amplitude, E_{Opt} is the optical gap, Γ is the broadening parameter, and ϕ is the phase of line shape, accounting for the effects of nonuniform fields and optical interference. The solid lines in Fig. 2c, d

represent the fitting results. The complete fitting results in pseudocolor 2D maps are provided in Supplementary Fig. 3.

The retrieved optical gaps for S-polarization (IP), denoted as $E_{\rm IP}$, are represented by blue triangles in Fig. 3a. $E_{\rm IP}$ increases from 1.3035 eV at 1 ps to 1.3051 eV at 7 ps, before decreasing to 1.3019 eV within 50 ps, showing a total variation of 3.2 meV. A similar trend is observed for the optical gaps for P-polarization (OP), $E_{\rm OP}$, shown by red triangles. $E_{\rm OP}$ rises from 1.3113 eV at 1 ps to 1.3131 eV at 7 ps, and then decrease to 1.3091 eV within 50 ps, with a variation of 4 meV. Notably, $E_{\rm OP}$ remains 6 ~ 8 meV higher than $E_{\rm IP}$ throughout the 150 ps time window. Additionally, both $E_{\rm IP}$ and $E_{\rm OP}$ are 13 ~ 24 meV lower than the exciton energies for IP and OP responses, 1.3262 eV and 1.3266 eV, respectively, as determined from the absorption spectra at 77 K (Supplementary Fig. 1).

Figure 3c illustrates the physical picture of exciton dynamics following photoexcitation in InSe. In the equilibrium state before time zero, $E_{\rm IP}$ and $E_{\rm OP}$ are the exciton energies, which are $R_{\rm ex,IP}$ and $R_{\rm ex,OP}$ lower than the CB edge, respectively. After the excitation by pump light, the optical gaps E_{OP} and $E_{\rm ID}$ are primarily influenced by three effects: the reduction of exciton binding energy, bandgap renormalization (BGR), and phase-space filling (PSF) effects. The reduction in exciton binding energy results from the dynamic screening of the Coulomb interaction caused by finite quasiparticle densities, which weakens the electron-hole attraction^{35–38}. BGR occurs due to photo-induced screening of Coulomb repulsion, leading to a decrease in the bandgap³⁵⁻⁴¹. PSF arises when high carrier densities fill available quantum states, causing Pauli blocking and a blue shift of the optical transition^{36,37,42}. As shown in Fig. 3c, BGR occurs immediately upon the presence of photocarriers, resulting in a redshift of the bandgap. Meanwhile, the varying reductions in exciton binding energies for IP and OP responses stem from the anisotropic screening of Coulomb interactions, leading to distinct IP and OP optical transitions with an energy difference ΔE . These effects cause a redshift of 13~24 meV in the optical gaps $E_{\rm IP}$ and $E_{\rm OP}$. Within 1 ps after photoexcitation, carriers rapidly exchange energy through carriercarrier scattering, during which the carrier temperature significantly exceeds the lattice temperature. The temporal variation in energies (3~4 meV) between 1 and 30 ps, as shown in Fig. 3a, is attributed to the PSF effects of excitons. After 1 ps, the thermal energy of the carriers decreases to below the exciton binding energy, resulting in efficient formation of excess excitons around the band edge⁴³. As the newly formed excitons sequentially fill higher excitonic states, E_{OP} and E_{IP} increase from 1 to 7 ps. Subsequently, the relaxation of excitons to lower excitonic states become more dominant

Fig. 3 | Exciton dynamics in InSe. a Optical gap energies and **b** broadening parameters extracted from the fits as a function of time delay for S- and P-polarized probes. c Schematic of exciton dynamics in InSe. $R_{\rm ex,IP}$ and $R_{\rm ex,OP}$ are exciton binding energies of the IP and OP responses, respectively. The purple arrow indicates pump excitation, while the blue and red arrows, labeled E_{IP} and E_{OP} , represent the optical gaps for the S- and P- polarized probes, respectively. The lengths of the arrows indicate the energy of the IP or OP optical gaps. Colored areas in the bands represent the energy distribution of occupied states. A slight blue shift is observed before 7 ps, resulting from exciton formation. Subsequently, the relaxation of excitons leads to redshift in the optical gaps.

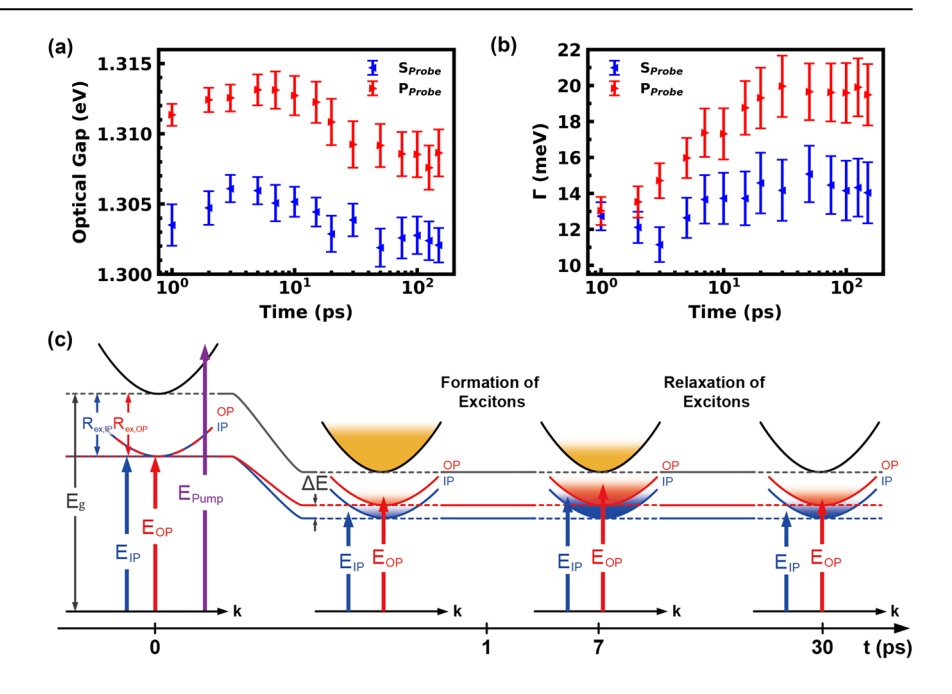
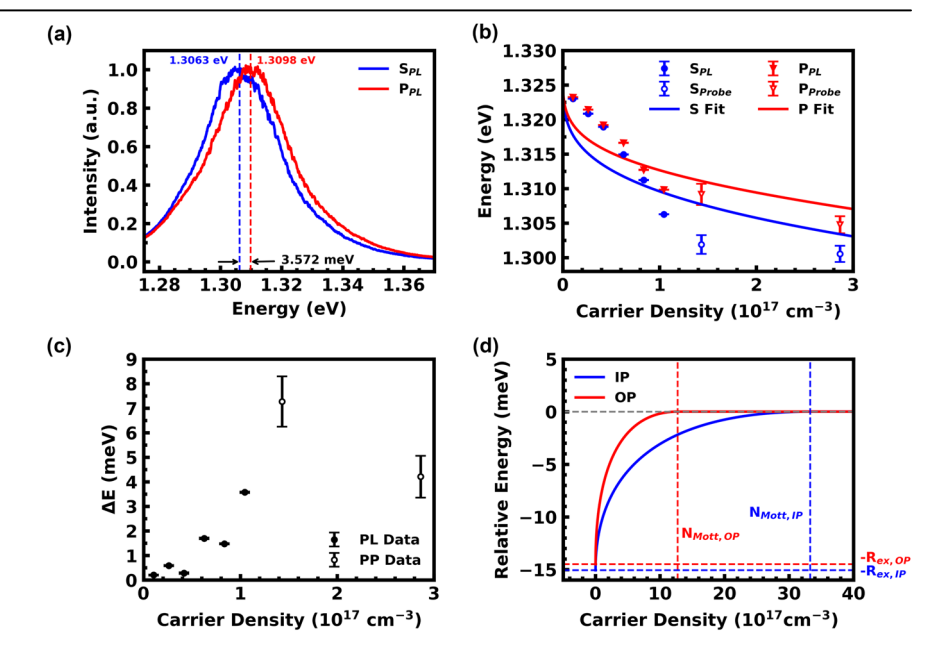


Fig. 4 | Dependence of carrier density on anisotropic screening of excitons. a Normalized S- and P-polarized PL spectra at a carrier density of 1.05 × 10¹⁷ cm⁻³. b PL peak energies and optical gaps (at 50 ps from pump-probe (PP) data) as a function of carrier density. c The energy difference between P- and S-polarized responses shown in (b). d The relative exciton energy as a function of carrier density. The horizontal dashed lines in gray, red, and blue color represent the bandgap, exciton energy for OP response, and exciton energy for IP response, respectively. The vertical dashed lines in red and blue indicate the Mott density for OP and IP responses, respectively.



than the formation of new excitons in higher energy states, leading to a decrease in $E_{\rm OP}$ and $E_{\rm IP}$ from 7 to 30 ps. We also observed that the broadening parameter Γ in Eq. (1) for both S- and P-polarizations increases from 1 to 30 ps, as shown in Fig. 3b. Exciton-exciton interactions cause spectral broadening due to enhanced scattering and dephasing processes as the number of excitons increases during this duration. After 30 ps, the optical gap slowly approaches the excitonic energies in equilibrium states on the order of nanosecond scales as the density of photoexcited carriers and excitons decreases.

Dependence of carrier density on anisotropic screening of excitons

The anisotropic reduction of exciton binding energies, due to the screening of photocarriers, was also observed in polarization-resolved PL with the geometry of oblique incidence. InSe samples at 77 K were excited using a 532 nm continuous-wave laser beam with P-polarization. Under the same

experimental conditions, a polarizer was rotated to record the PL spectra for both S- and P-polarizations. Figure 4a shows the normalized PL spectra, revealing that the peak of the S-polarized PL is 3.6 meV lower than that of the P-polarized PL, attributed to the different screening energies of excitons for IP and OP responses. The S- and P-polarized PL spectra for different carrier density were presented in Supplementary Figs. 4 and 5. The peak energies of the PL spectra are plotted as solid dots and triangles in Fig. 4b for carrier density ranging from 10^{16} to 10^{17} cm⁻³. Additionally, the optical gaps at 50 ps from the pump-probe (PP) data (from Fig. 3a with a carrier density of 1.43×10^{17} cm⁻³, and Supplementary Fig. 7a with a carrier density of 2.86×10^{17} cm⁻³) are also shown in the same figure. Both the energies for S- and P-polarizations decrease with increasing carrier density. Figure 4c reveals the energy difference in Fig. 4b ($\Delta E = E_{\rm OP} - E_{\rm IP}$) as a function of carrier density.

As previously discussed, the variation of optical gap (or PL peak energy) is influenced by BGR, PSF, and exciton binding energy, all of which depend on carrier density. However, only the reduction in exciton binding

energy due to anisotropic screening accounts for ΔE in Fig. 4c for S- and P-polarized measurements. The carrier dependence of ΔE can be attributed to the varying screening effects caused by different dielectric constants of InSe along the IP and OP directions. However, it is still challenging to investigate anisotropic screening effect by using an analytical model or first-principles calculations. Here, we consider homogeneous screening of excitons in two distinct media and calculate the energy difference. The reduction in exciton binding energy is associated with screened Coulomb interactions, which can be described by the Yukawa potential ⁴⁴. Approximating the Yukawa potential with the Hulthén potential, the ground-state exciton binding energy under screening can be expressed as ref. 44:

$$E_s = \begin{cases} \left(1 - a_0/\lambda_s\right)^2 R_{\text{ex}}, & \text{if } \lambda_s \ge a_0 \\ 0, & \text{if } \lambda_s < a_0 \end{cases}$$
(2)

where a_0 is the exciton Bohr radius, $R_{\rm ex}$ is the exciton binding energy without screening, and $\lambda_{\rm s}$ is the screening length, which is given by refs. 44,45:

$$\lambda_s = \sqrt{\frac{\varepsilon_r \varepsilon_0}{2e^2} \frac{\partial \mu}{\partial N}}.$$
 (3)

Here, $\varepsilon_{\rm r}$ is the relative dielectric constant, ε_0 is the vacuum permittivity, μ is the chemical potential, e is the charge of an electron. In the classical high-temperature limit, particles follow a Boltzmann distribution, reducing Eq. (3) to the Debye-Hückel screening length, where $\partial \mu/\partial N$ is approximated to be $k_B T/N^{44,45}$. As the carrier density N increases from zero, the term a_0/λ_s in Eq. (2) increases from zero, leading to a reduction in exciton binding energy. When a_0/λ_s reaches 1 (or $\lambda_s=a_0$), N reaches the Mott density $N_{\rm Mott}$, at which point E_s becomes zero, and the excitons dissociate.

The $\varepsilon_{\rm r}$ of InSe in the IP and OP directions $\varepsilon_{\rm r,IP}$ and $\varepsilon_{\rm r,OP}$ are 10.2 and 7.6, respectively 46. Additionally, $\epsilon_{\rm r}a_0=R_{\rm ex}R_{\rm H}a_{\rm H}$, where $a_{\rm H}$ and $R_{\rm H}$ are the Bohr radius and Rydberg energy of a hydrogen atom, respectively. The Bohr radii of excitons for IP and OP responses, $a_{0,\mathrm{IP}}$ and $a_{0,\mathrm{OP}}$, are thus obtained to be 4.68 nm and 6.53 nm, respectively. Using these constants, the relative energy $(-E_s)$ as a function of carrier density N is calculated based on Eqs. (2) and (3), as shown in Fig. 4d. The screen length λ_s as a function of N is shown in Supplementary Fig. 8. The Mott densities for IP $(N_{\rm Mott,IP}=3.33\times 10^{18}~{\rm cm^{-3}})$ and OP $(N_{\rm Mott,OP}=1.27\times 10^{18}~{\rm cm^{-3}})$ are marked in the figures for reference. Since $\varepsilon_{r,OP}$ is smaller than $\varepsilon_{r,IP}$, the binding energy of excitons for OP response decreases more rapidly with increasing N than that for IP response, causing ΔE to increase. However, as N approaches the $N_{\text{Mott,OP}}$, the reduction in exciton binding energy slows, and ΔE begins to decrease before $N_{\rm Mott, OP}$ is reached. Once N exceeds both $N_{\text{Mott,OP}}$ and $N_{\text{Mott,IP}}$, ΔE reaches zero. Although we consider the energy difference of homogenous excitons in varying media with distinct dielectric constants, which differs from the actual condition of anisotropic excitons in birefringent materials, this simplified analytical calculation is still capable of explaining the experimental data in Fig. 4c, where ΔE first increases and then decreases with increasing carrier density.

To further quantitatively understand the dependence of carrier density on energy in Fig. 4b, the effects of BGR, PSF, and exciton binding energy should all be considered. The energy in the presence of photocarriers can be expressed as:

$$E_{\rm Opt} = \Delta E_{\rm BGR} + \Delta E_{\rm PSF} + \Delta E_{\rm ex} + E_{\rm ex}, \tag{4}$$

where $\Delta E_{\rm BGR}$, $\Delta E_{\rm PSF}$, and $\Delta E_{\rm ex}$ represent the energy shifts due to BGR, PSF, and exciton screening, respectively. $E_{\rm ex}$ is the exciton energy without photocarriers. For BGR, $\Delta E_{\rm BGR} = -A_{\rm BGR} N^{1/3}$, where $A_{\rm BGR}$ is a constant ⁴⁷. For PSF, we use the Burstein-Moss (BM) band-filling effect ⁴⁸, described by $\Delta E_{\rm PSF} = A_{\rm PSF} N^{2/3}$, where $A_{\rm PSF}$ is another constant. The energy shift due to exciton screening is $\Delta E_{\rm ex} = R_{\rm ex} - E_{\rm s}$. Using the experimentally determined exciton energies at 77 K and treating $A_{\rm BGR}$ and $A_{\rm PSF}$ as fitting parameters,

the solid lines in Fig. 4b show the fitting results of Eq. (4). The values of $A_{\rm BGR}$ for the IP (4.60 × 10⁻⁸ eV-cm) and OP (4.53 × 10⁻⁸ eV-cm) cases are nearly identical, confirming that BGR is independent of light polarization. The $A_{\rm PSF}$ values for both the IP and OP cases are close to zero, indicating that the PSF effect is negligible. The contributions of the three effects are shown in Supplementary Fig. 9, where BGR (resulting in a redshift) dominates the overall behavior. In Fig. 4b, the energy redshifts by up to 23 meV at \sim 3 × 10¹⁷ cm⁻³. Given that exciton screening causes a blue shift of up to \sim 10 meV, the maximum redshifted energy due to BGR exceeds 30 meV under our experimental conditions.

IP and OP optical transitions at RT

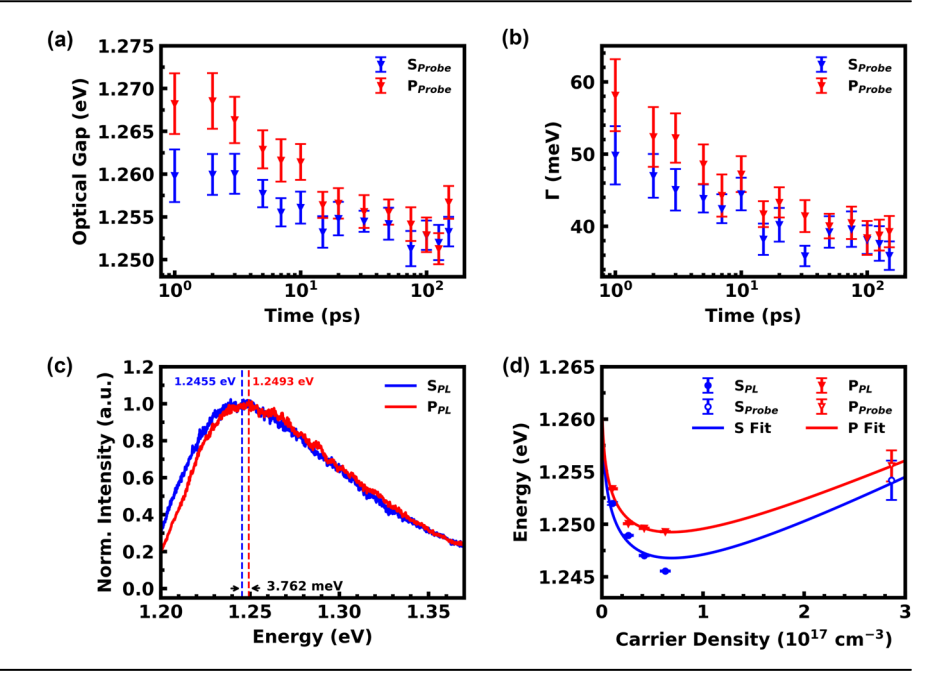
Similar measurements were conducted at RT (294 K). As with Fig. 2 at 77 K, time-resolved ΔR/R spectra for S- and P-polarized probes at RT are shown in Supplementary Fig. 10 and were fitted using Eq. (1). Figure 5a shows the extracted optical gaps $E_{\rm IP}$ and $E_{\rm OP}$ as a function of time. The energy difference ΔE , resulting from the anisotropic screening of excitons, is also observable at RT. However, it gradually decreases from 8 meV at 1 ps to 1.3 meV at 50 ps, becoming indistinguishable after 100 ps. In contrast, at 77 K, ΔE remains 6 ~ 8 meV over 100 ps (Fig. 3a). In addition, both $E_{\rm IP}$ and E_{OP} at RT decrease from 1 ps to 15 ps, which differs from the behavior at 77 K, where they increase from 1 ps to 7 ps and then decrease until 30 ps. The temperature-dependent phenomena are attributed to the lifetime of excitons. At RT, the thermal energy (25.4 meV) exceeds the exciton binding energy in InSe (~15 meV), unlike at 77 K (6.6 meV). After photoexcitation at 3.1 eV, hot carriers thermalize through carrier-carrier and carrierphonon scattering processes. These thermalized carriers cannot efficiently form additional excitons. Additionally, the originally formed excitons dissociate more easily due to the higher thermal energy and scattering processes at RT. As a result, the thermalization and dissociation of excitons dominate the temporal changes in $E_{\rm IP}$ and $E_{\rm OP}$ within the first 15 ps. These processes also contribute to a decrease in the broadening parameter Γ , as shown in Fig. 5b³⁸. When $\Delta E \sim 0$, the dynamics is dominated by free carriers in the CB and VB, rather than excitons, because the optical gap due to free carriers is independent of probe polarization.

Figure 5c shows the normalized PL spectra for S- and P-polarization at RT. The PL spectra should consist of luminescence from the radiative recombination of excitons and free carriers. The right portions of both spectra, which primarily result from the recombination of free carriers, almost overlap. But the difference on the left side, due to anisotropic screening of excitons, remains distinguishable, even though excitons easily dissociate at RT. Power-dependent PL spectra are presented in Supplementary Figs. 11 and Fig. 12. Figure 5d shows the dependence of carrier density on the peak energy of the PL spectra. The optical gap at 50 ps from Fig. 5a is also included. In contrast to Fig. 4b, which shows a consistent redshift at 77 K, the energy initially decreases but then increases. Because BM band-filling effect dominates at RT rather than PSF effect, ΔE_{PSF} in Eq. (4) is replaced by $\Delta E_{\rm BM} = A_{\rm BM} N^{2/348}$, where $A_{\rm BM}$ is a constant, to fit the data. By treating $A_{\rm BGR}$ and $A_{\rm BM}$ as fitting parameters, the fitting results are indicated by the solid lines of Fig. 5d. Individual contributions of $\Delta E_{\rm BGR},$ $\Delta E_{\rm BM}$, and $\Delta E_{\rm ex}$ are presented in Supplementary Fig. 14. The IP and OP values of $A_{\rm BGR}$ are 9.98×10^{-8} eV-cm and 9.01×10^{-8} eV-cm, respectively, while the values of $A_{\rm BM}$ for the IP and OP cases are 1.12×10^{-13} eV-cm² and 0.97×10^{-13} eV-cm². Regarding the screening of excitons, the calculated Mott densities of IP and OP excitons at RT are both ~3.8 times higher than those at 77 K. This indicates that the screening effect is reduced at RT. Therefore, for the same carrier density, $\Delta E_{\rm ex}$ increases by up to ~ 5 meV at RT, in contrast to ~10 meV at 77 K.

Discussion

We found that the excitons near the bandgap in InSe are not only anisotropic in their oscillation strength but also in their energy. Although the energy difference between the IP and OP optical responses from excitons in InSe is small, they originate from different composite electronic states. Notably, we observed that this energy difference depends on carrier

Fig. 5 | IP and OP optical transitions at RT. a Optical gap energies and b broadening parameters extracted from the fits as a function of time delay for S- and P-polarized probes. c Normalized S- and P-polarized PL spectra at a carrier density of 6.27 × 10¹⁶ cm⁻³. d PL peaks and optical gaps (at 50 ps from PP measurements) as a function of carrier density.



density, with photocarriers increasing the energy difference by as much as 8 meV. The anisotropic energy responses arise from variations in the screening effects of photocarriers on excitons along the IP and OP directions. Since the dielectric constant of InSe in the OP direction is lower than that in the IP direction, the exciton binding energy decreases more rapidly in the OP direction before reaching the Mott density. At 77 K, the energy difference due to anisotropic screening of excitons persists for over 100 ps after the excitation of photocarriers. However, at RT, where the thermal energy exceeds exciton binding energy, anisotropic screening of excitons remains observable. It requires a higher carrier density at RT than at low temperatures to achieve the same reduction in exciton binding energy. Given that the anisotropic screening of excitons is attributed to the optical birefringence, this phenomenon should be universal in vdW or 2D materials.

Methods

First-principles calculations

The density functional theory calculations were performed using the Quantum Espresso package⁴⁹ with the generalized gradient approximation to the exchange-correlation functional. The DFT-D3 correction was used to describe the vdW interaction. The lattice constant was adopted from the experiment⁵⁰. An 80 Ry energy cutoff was applied to wavefunctions with a 6 × 6 × 6 k-point sampling of the BZ. SOC was included in all the calculations. The DFT wavefunctions are used as the mean-field starting point for quasiparticle GW and GW-BSE studies, using the BerkeleyGW package⁵¹. In the construction of the GW self-energy, we adopt the Hybertsen-Louie generalized plasmon-pole model⁵² for the frequency dependence in the inverse dielectric matrix, which was constructed with a 15 Ry cutoff. The inverse dielectric matrix and the self-energy operator were constructed with a summation up to 1200 bands. In constructing the BSE Hamiltonian, the electron-hole matrix elements were initially calculated on a $6 \times 6 \times 6$ coarse grid, and then interpolated to an effective 120 × 120 × 120 sampling using a patched-sampling technique that focuses on a small region in the BZ of interest⁵³.

Crystal growth

To prepare the InSe single crystals, we used 99.999% pure molar mixture of In (52.4% weight percentage) and Se (47.6%) compounds. The synthesis of single-crystalline InSe powder was performed in conical quartz ampoules evacuated to 10^{-4} Pa. Homogenization of the batches and synthesis of the

InSe powder were conducted in a horizontal furnace at 600 °C for 48 h. The mixed crystals were grown using the vertical Bridgman method. Before pulling, the ampoules containing the melt were heat-treated at 850 °C for 24 h; when the melt filled the tip of ampoule, the ampoules were lowered through a temperature gradient of 1 °C at a rate of 0.1 mm/h. The obtained InSe single crystals were 3 cm long and 1.2 cm in diameter. The as-grown crystals of excellent optical quality were easy to cleave to obtain crystalline planes perpendicular to the trigonal c axis. Powder X-ray diffraction (PXRD) analysis identified the lattice structure as γ -phase (R3m), with an OP lattice constant of c = 2.4969 nm and hexagonal parameters a = b = 0.4006 nm. Oblique incident SHG measurements further confirmed the γ -phase of the samples ⁵⁴.

Absorption measurements

Transmission spectra were measured using a custom-built setup with a micron-sized optical spot focused on the InSe flakes on sapphire substrates. The broadband transmitted light was collected through a multi-mode fiber coupled to a spectrometer (iHR550, HORIBA), allowing absorption spectra to be derived using the Beer-Lambert law 55 . The cryostat was tilted at an angle of $\sim\!22^{\circ}$, with a polarizer placed in front of the sample for S- and P-polarized measurements.

Ultrafast pump-probe measurements

Ti:sapphire ultrafast laser system was utilized to perform oblique pumpprobe TR spectroscopy. The repetition rate was 80 MHz and the central energy was ~1.55 eV. The pump beam was frequency-doubled with a beta barium borate (BBO) crystal, modulated with an acousto-optical modulator (AOM) at 100 kHz, and directed through a motorized delay stage for controlling the time delay between the pump and probe pulses. A half-wave plate (10RP02-41, Newport) and a polarizer (10LP-UV, Newport) were placed in the path to change the polarization of the pump beam. The supercontinuum probe beam is generated by a photonic crystal fiber (PCF, SCG-800, Newport). Optical filters (FGL610, Thorlabs, and LP02-785-RE-25, Semrock) were utilized to block the extra wavelength of the probe beam. The polarization of the probe beam was adjusted using a half-wave plate (10RP42-4, Newport) and a polarizer (WP25M-UB, Thorlabs). The pump and probe beams were recombined collinearly with a dichroic mirror (Di02-R830-25 × 36, Semrock). The collinear pump/probe beams were focused onto the samples, using a lens (54-17-29 UV, Special Optics). The radius of the focused spots was \sim 13 μ m. The cryostat with InSe samples was tilted at an angle of ~51°. The reflected signal was collimated by a lens (54-18-23 IR, Special Optics), passed through a monochromator (SpectraPro-2500i, Acton), and finally sensed by a Photomultiplier (PMT) (R5108, Hamamatsu). The selected energy of the signal ranged from 1.210 eV to 1.345 eV at RT and from 1.270 to 1.395 eV at 77 K. The spectral resolution was ~1 nm. The photocurrent signals were demodulated using a lock-in amplifier (SR844, Stanford Research Systems) to extract the signal ΔR . This signal was divided by R, obtained by modulating the probe beam in the absence of the pump beam. The duration of the cross-correlation of pump/ probe beams was ~1 ps. The imaging system, positioned at the back of the cryostat, was utilized to precisely locate both the samples and the laser beam.

PL measurements

A cw 532 nm laser (GLK-32200-TS, LASOS) served as the excitation source. The laser beam passed through a laser line filter (532BPF, IRI-DIAN) to ensure a clean laser wavelength. Subsequently, a half-wave plate (WPH10M-532, Thorlabs) and a polarizer (WP25M-VIS, Thorlabs) were used to adjust the incident polarization. The laser beam was then focused onto the sample by a lens (54-17-29 UV, Special Optics), producing a focused spot with a radius of ~4.2 μm . The cryostat with InSe samples was tilted at an angle of 45°. The reflected light, including the PL, was collimated by another lens (54-18-23 IR, Special Optics) and passed through a polarizer (WP25M-UB, Thorlabs) and two edge filters (532Edge, IRI-DIAN, and LP02-532RE-25, Semrock). Finally, a lens (LA4148, Thorlabs) focused the luminescence light into a multi-mode fiber, coupled to a spectrometer (iHR550, HORIBA). An imaging system was set at the back of the cryostat to identify the positions of both the samples and the laser beam.

Data availability

The data that support the findings of this study are available from the corresponding author upon reasonable request.

Code availability

The codes that support the findings of this study are available from the corresponding author upon reasonable request.

Received: 1 November 2024; Accepted: 29 April 2025; Published online: 12 May 2025

References

- Basu P. K. Theory of optical processes in semiconductors: bulk and microstructures. (Oxford University Press, 2003).
- Wang, G. et al. In-plane propagation of light in transition metal dichalcogenide monolayers: optical selection rules. *Phys. Rev. Lett.* 119, 047401 (2017).
- Xiao, J., Zhao, M., Wang, Y. & Zhang, X. Excitons in atomically thin 2D semiconductors and their applications. *Nanophotonics* 6, 1309–1328 (2017).
- Do, D. T., Mahanti, S. D. & Lai, C. W. Spin splitting in 2D monochalcogenide semiconductors. Sci. Rep. 5, 17044 (2015).
- Schuller, J. A. et al. Orientation of luminescent excitons in layered nanomaterials. *Nat. Nanotechnol.* 8, 271–276 (2013).
- Scott, R. et al. Directed emission of CdSe nanoplatelets originating from strongly anisotropic 2D electronic structure. *Nat. Nanotechnol.* 12, 1155–1160 (2017).
- 7. Guilhon, I. et al. Out-of-plane excitons in two-dimensional crystals. *Phys. Rev. B* **99**, 161201 (2019).
- 8. Brotons-Gisbert, M. et al. Out-of-plane orientation of luminescent excitons in two-dimensional indium selenide. *Nat. Commun.* **10**, 3913 (2019)
- Gong, C. et al. Electronic and optoelectronic applications based on 2D novel anisotropic transition metal dichalcogenides. Adv. Sci. 4, 1700231 (2017).

- Mak, K. F. & Shan, J. Photonics and optoelectronics of 2D semiconductor transition metal dichalcogenides. *Nat. Photonics* 10, 216–226 (2016).
- Song, X. et al. Progress of large-scale synthesis and electronic device application of two-dimensional transition metal dichalcogenides. Small 13, 1700098 (2017).
- Kravets, V. G., Zhukov, A. A., Holwill, M., Novoselov, K. S. & Grigorenko, A. N. Dead" exciton layer and exciton anisotropy of bulk MoS₂ extracted from optical measurements. ACS Nano 16, 18637–18647 (2022).
- Andres-Penares, D. et al. Out-of-plane trion emission in monolayer WSe₂ revealed by whispering gallery modes of dielectric microresonators. Commun. Mater. 2, 52 (2021).
- You, J. et al. Hybrid/integrated silicon photonics based on 2D materials in optical communication nanosystems. *Laser Photonics Rev.* 14, 2000239 (2020).
- Xu, K. et al. Strong linearly polarized light emission by coupling out-ofplane exciton to anisotropic gap plasmon nanocavity. *Nano Lett.* 24, 3647–3653 (2024).
- Bao, X. et al. Giant out-of-plane exciton emission enhancement in two-dimensional indium selenide via a plasmonic nanocavity. *Nano Lett.* 23, 3716–3723 (2023).
- Borghardt, S. et al. Radially polarized light beams from spin-forbidden dark excitons and trions in monolayer WSe₂. Opt. Mater. Express 10, 1273–1285 (2020).
- Li, Y. et al. Enhanced light emission from the ridge of two-dimensional InSe flakes. Nano Lett. 18, 5078–5084 (2018).
- Mazumder, D. et al. Enhanced optical emission from 2D InSe bent onto Si-pillars. Adv. Opt. Mater. 8, 2000828 (2020).
- Xie, J. & Zhang, L. Optical emission enhancement of bent InSe thin films. Sci. China Inf. Sci. 64, 140405 (2021).
- Brotons-Gisbert, M. et al. Nanotexturing to enhance photoluminescent response of atomically thin indium selenide with highly tunable band gap. *Nano Lett.* 16, 3221–3229 (2016).
- Bandurin, D. A. et al. High electron mobility, quantum Hall effect and anomalous optical response in atomically thin InSe. *Nat. Nanotechnol.* 12, 223–227 (2017).
- Sucharitakul, S. et al. Intrinsic electron mobility exceeding 10³ cm²/(V s) in multilayer InSe FETs. Nano Lett. 15, 3815–3819 (2015).
- 24. Wang, F. et al. Piezopotential gated two-dimensional InSe field-effect transistor for designing a pressure sensor based on piezotronic effect. *Nano Energy* **70**, 104457 (2020).
- Wang, X. et al. Strong anisotropy of multilayer γ-InSe-enabled polarization division multiplexing photodetection. *Adv. Photonics Res.* 3, 2200119 (2022).
- Tamalampudi, S. R. et al. High performance and bendable fewlayered InSe photodetectors with broad spectral response. *Nano Lett.* 14, 2800–2806 (2014).
- Zhang, L. et al. Optoelectronic gas sensor based on few-layered InSe nanosheets for NO₂ detection with ultrahigh antihumidity ability. *Anal. Chem.* 92, 11277–11287 (2020).
- Song, C. et al. Largely tunable band structures of few-layer InSe by uniaxial strain. ACS Appl. Mater. Interfaces 10, 3994–4000 (2018).
- Ermolaev, G. A. et al. Giant optical anisotropy in transition metal dichalcogenides for next-generation photonics. *Nat. Commun.* 12, 854 (2021).
- Slavich, A. S. et al. Exploring van der Waals materials with high anisotropy: geometrical and optical approaches. *Light. Sci. Appl.* 13, 68 (2024).
- 31. Fox A. M. Optical properties of solids (Oxford University Press, 2001).
- 32. Camassel, J., Merle, P., Mathieu, H. & Chevy, A. Excitonic absorption edge of indium selenide. *Phys. Rev. B* 17, 4718–4725 (1978).
- Shubina, T. V. et al. InSe as a case between 3D and 2D layered crystals for excitons. Nat. Commun. 10, 3479 (2019).

- Pollak, F. H. & Glembocki, O. J. Modulation spectroscopy of semiconductor microstructures: an overview. *Proc. SPIE* 0946, 2 (1988).
- Gao, S., Liang, Y., Spataru, C. D. & Yang, L. Dynamical excitonic effects in doped two-dimensional semiconductors. *Nano Lett.* 16, 5568–5573 (2016).
- Cunningham, P. D., Hanbicki, A. T., McCreary, K. M. & Jonker, B. T. Photoinduced bandgap renormalization and exciton binding energy reduction in WS₂. ACS Nano 11, 12601–12608 (2017).
- Aivazian, G. et al. Many-body effects in nonlinear optical responses of 2D layered semiconductors. 2D Mater. 4, 025024 (2017).
- Suk, S. H., Seo, S. B., Cho, Y. S., Wang, J. & Sim, S. Ultrafast optical properties and applications of anisotropic 2D materials. *Nanophotonics* 13, 107–154 (2024).
- Pogna, E. A. A. et al. Photo-induced bandgap renormalization governs the ultrafast response of single-layer MoS₂. ACS Nano 10, 1182–1188 (2016).
- Chang, Q. et al. Tracking carrier and exciton dynamics in mixed-cation lead mixed-halide perovskite thin films. Commun. Phys. 5, 187 (2022).
- Wu, T.-H. et al. Ultrafast carrier dynamics and layer-dependent carrier recombination rate in InSe. Nanoscale 15, 3169–3176 (2023).
- 42. Yan, T., Yu, H., Xiao, K., Yao, W. & Cui, X. Probing the exciton k-space dynamics in monolayer tungsten diselenides. *2D Mater.* **6**, 025035 (2019).
- Nüsse, S., Haring Bolivar, P., Kurz, H., Klimov, V. & Levy, F. Carrier cooling and exciton formation in GaSe. *Phys. Rev. B* 56, 4578–4583 (1997).
- 44. Versteegh, M. A. M., Kuis, T., Stoof, H. T. C. & Dijkhuis, J. I. Ultrafast screening and carrier dynamics in ZnO: theory and experiment. *Phys. Rev. B* **84**, 035207 (2011).
- 45. Haug H., Koch S. W. Quantum theory of the optical and electronic properties of semiconductors. World Scientific (2004).
- Manjón, F. J., Vijver, Yvd, Segura, A. & Muñoz, V. Pressure dependence of the refractive index in InSe. Semicond. Sci. Technol. 15, 806 (2000).
- Berggren, K. F. & Sernelius, B. E. Band-gap narrowing in heavily doped many-valley semiconductors. *Phys. Rev. B* 24, 1971–1986 (1981).
- Fu, J., Ramesh, S., Melvin Lim, J. W. & Sum, T. C. Carriers, quasiparticles, and collective excitations in halide perovskites. *Chem. Rev.* 123, 8154–8231 (2023).
- Giannozzi, P. et al. Advanced capabilities for materials modelling with quantum ESPRESSO. J. Phys.: Condens. Matter 29, 465901 (2017).
- Rigoult, J., Rimsky, A. & Kuhn, A. Refinement of the 3Rγ-indium monoselenide structure type. *Acta Crystallogr. Sect. B* 36, 916–918 (1980).
- Deslippe, J. et al. BerkeleyGW: a massively parallel computer package for the calculation of the quasiparticle and optical properties of materials and nanostructures. *Comput. Phys. Commun.* 183, 1269–1289 (2012).
- Hybertsen, M. S. & Louie, S. G. Electron correlation in semiconductors and insulators: band gaps and quasiparticle energies. *Phys. Rev. B* 34, 5390–5413 (1986).
- 53. Alvertis, A. M. et al. Importance of nonuniform Brillouin zone sampling for ab initio Bethe-Salpeter equation calculations of exciton binding energies in crystalline solids. *Phys. Rev. B* **108**, 235117 (2023).
- Li, Z.-Y. et al. Uniaxial strain dependence on angle-resolved optical second harmonic generation from a few layers of indium selenide. *Nanomaterials* 13, 750 (2023).

 Nama Manjunatha, K. & Paul, S. Investigation of optical properties of nickel oxide thin films deposited on different substrates. *Appl. Surf.* Sci. 352, 10–15 (2015).

Acknowledgements

C.-C.L. acknowledges support from the National Science and Technology Council (NSTC) of Taiwan under No. 113-2112-M-032-004 and from the National Center for Theoretical Sciences (NCTS) of Taiwan. R.S. acknowledges support from NSTC of Taiwan under No. 111-2124-M-001-007, 113-2112-M-001-045-MY3, and Academia Sinica Project No. AS-iMATE-113-12. Z.L. is supported by the Zumberge Preliminary Studies Research Award at the University of Southern California. C.-S.C. acknowledges support from the NSTC of Taiwan under No. 112-2112-M-001-078. K.-H.L. acknowledges support from NSTC of Taiwan under No. 113-2112-M-001-056, 113-2124-M-001-019, 113-2124-M-001-013-MY3. R.K.U. would like to acknowledge the IITR for the Faculty Initiation Grant (No. FIG-101068).

Author contributions

K.-H.L. and T.-H.W. conceived this work. K.H.L. and C.S.C. supervised this work. T.-H.W. performed the experiments and analyzed the data. C.-E. H., Z.L., and C.-C.L. performed the theoretical calculations. R.K.U. and R.S. grew the crystals. K.-H.L. and T.-H.W. wrote the draft and finalized the manuscript.

Competing interests

The authors declare no competing interests.

Additional information

Supplementary information The online version contains supplementary material available at https://doi.org/10.1038/s41699-025-00565-1.

Correspondence and requests for materials should be addressed to Kung-Hsuan Lin.

Reprints and permissions information is available at http://www.nature.com/reprints

Publisher's note Springer Nature remains neutral with regard to jurisdictional claims in published maps and institutional affiliations.

Open Access This article is licensed under a Creative Commons Attribution-NonCommercial-NoDerivatives 4.0 International License, which permits any non-commercial use, sharing, distribution and reproduction in any medium or format, as long as you give appropriate credit to the original author(s) and the source, provide a link to the Creative Commons licence, and indicate if you modified the licensed material. You do not have permission under this licence to share adapted material derived from this article or parts of it. The images or other third party material in this article are included in the article's Creative Commons licence, unless indicated otherwise in a credit line to the material. If material is not included in the article's Creative Commons licence and your intended use is not permitted by statutory regulation or exceeds the permitted use, you will need to obtain permission directly from the copyright holder. To view a copy of this licence, visit http://creativecommons.org/licenses/by-nc-nd/4.0/.

© The Author(s) 2025